

# Conformational Space of (1R,2S)-Dimethyl-Ephedrinium and (1S,2S)-Dimethyl-Pseudoephedrinium in the Synthesis of Nanoporous Aluminophosphates

*Beatriz Bernardo-Maestro,<sup>a</sup> Pilar Gálvez,<sup>a</sup> Dorleta González,<sup>a</sup> Fernando López-Arbeloa,<sup>b</sup> Joaquín Pérez-Pariente,<sup>a</sup> and Luis Gómez-Hortigüela<sup>a,\*</sup>*

<sup>a</sup> Instituto de Catálisis y Petroleoquímica, ICP-CSIC. C/ Marie Curie 2, 28049. Madrid, Spain.

<sup>b</sup> Departamento de Química Física. Universidad del País Vasco. Apartado 644, 48080-Bilbao, Spain.

Corresponding Author: LGH; Email: [lhortiguela@icp.csic.es](mailto:lhortiguela@icp.csic.es)

Telephone: +34-91-5854785; Fax: +34-91-5854760.

**Abstract.** In this work we report a comparative study about the structure-directing effect of two chiral diastereoisomers, (1R,2S)-dimethyl-ephedrinium and (1S,2S)-dimethyl-pseudoephedrinium, for the synthesis of nanoporous aluminophosphates. Both isomers direct the crystallization of the one-dimensional channels composing the AFI framework in the presence of divalent dopants when the crystallization temperature is moderate (140 °C). An increase of the crystallization temperature (to 180 °C) severely limits the structure-directing ability towards the AFI framework because of a poor

hydrothermal stability of the organic cations, especially of the (1S,2S)-isomer.  $^{13}\text{C}$  NMR and molecular simulations studies of these organic cations in solution and confined within nanoporous zeolitic materials allow us to clearly identify  $^{13}\text{C}$  resonance signals of particular methyl groups which vary as a function of the conformational space, and enable us to monitor the occurrence of the different conformers in diverse environments. In vacuo and in solution, both organic cations display a conformation with an open-configuration, in which the bulky phenyl and trimethylammonium groups site in ‘anti’ configuration. Such conformational space is altered when the cations are confined within the limited space of the one-dimensional channels of the AFI structure. In this case, despite folded-conformations being intrinsically less stable, lateral packing interactions within the channels drive an incorporation of the cations as a mixture of conformers (with open- and folded-configurations) for the (1R,2S)-isomer or as folded conformers for the (1S,2S)-isomer, showing the importance of the conformational space of organic cations during the structure-directing phenomenon.

## **Introduction**

Nanoporous materials, and in particular zeolite and zeolite-related materials, have found many different applications in the chemical industry due to their particular properties, which include cationic-exchange, molecular sieving and catalytic capacities.<sup>1-3</sup> All these capacities are a consequence of the particular framework structure of zeolites, which exploit the molecular dimensions of the nanoporous frameworks to discriminate between guest species (sorbates, reactants, transition states or products) with even small steric differences.<sup>4</sup> Indeed, zeolites have had a profound impact on the chemical industry sector, especially in the petrochemical sector, because of their use as acid heterogeneous catalysts, greatly improving the sustainability of the associated chemical

processes.<sup>5,6</sup> A related family of zeolite materials is provided by nanoporous aluminophosphates (AlPO<sub>4</sub>), where SiO<sub>4</sub> tetrahedra are substituted by alternated AlO<sub>4</sub> and PO<sub>4</sub> tetrahedra, giving particular chemical properties to these networks different from those of silica-based zeolites.<sup>7</sup> For instance, the particular chemistry of the AlPO<sub>4</sub> network enables a versatile incorporation of different catalytic active sites by replacement of either Al, P or both, leading to efficient catalysts in different types of reactions.<sup>8</sup>

In this context, the control of the zeolite porous architecture is crucial for the adequate functioning of a zeolite material in a particular chemical process which would benefit from the shape-selectivity properties of its particular framework structure. Hence, it is essential to control the crystallization of particular zeolite architectures during the synthesis of these materials. Such control has been mostly achieved through the use of organic structure-directing agents (SDA), which are organic (generally cationic) species which are added to the zeolite synthesis gels in order to direct the crystallization pathway towards a particular framework type.<sup>9-13</sup> These organic species organize the inorganic tetrahedral units around themselves in a particular geometry, giving place to precursors from which nucleation and crystal growth will take place. There is usually (but not always) a geometrical relationship between the SDA and the porous architecture of the resulting zeolite, and for this reason SDAs are also said to act as templates of zeolite frameworks.<sup>14</sup> By carefully-designing the molecular size and shape of the organic species to be used as SDAs, one can at least partially control the porous framework to be obtained.<sup>15</sup>

One of the most challenging uses of organic SDAs in zeolite science is to promote the crystallization of chiral frameworks.<sup>16,17</sup> Chiral zeolites are one of the most highly-desired targets in materials science, since their confinement effect in nanoporous spaces

could potentially enhance their enantioselective properties, and hence they could provide with environmentally-friendly heterogeneous enantioselective catalysts, which would have a great impact in the chemical industry, especially in the pharmaceutical sector.<sup>18-22</sup> Indeed, several chiral zeolite frameworks do actually exist,<sup>21,23-27</sup> although they usually crystallize as racemic mixtures (either racemic conglomerates like STW or racemic compounds like \*BEA). Due to the usual geometrical and spatial relationship between organic SDAs and the porous system of the zeolite materials that crystallize in their presence, the straightforward strategy to promote the crystallization of chiral zeolite frameworks is through the use of chiral organic species as SDAs, in an attempt to transfer the chirality from the molecular component to the porous architecture following the concept of ‘template’ effect.<sup>28</sup> However, despite the wide use of chiral SDAs, there has been very scarce achievement in producing chiral zeolites. Nonetheless, there is a recent example of enantio-enrichment of a chiral zeolite (STW) through the use of rationally-designed chiral organic structure-directing agents,<sup>29</sup> demonstrating the viability of this strategy.

In our group, we have been working for some time with derivatives of chiral alkaloids (1R,2S)-ephedrine and (1S,2S)-pseudoephedrine to promote the crystallization of zeolitic nanoporous materials, especially in  $\text{AlPO}_4$  composition.<sup>30-33</sup> Our rationale behind this choice is that these chiral (easily-available) species can promote the development of supramolecular helicoidal arrangements that can be transferred to the nascent zeolite framework, either to the overall nanoporous architecture (giving a chiral framework) or to the spatial distribution of dopants embedded in achiral networks.<sup>34</sup> On the course of our investigations, we found that (1R,2S)-dimethylephedrinium (DMEP) direct the crystallization of the AFI framework in the presence of Mg;<sup>35</sup> the AFI structure is composed of one-dimensional 12-ring cylindrical channels with a diameter

of 7.3 Å.<sup>36</sup> On the other hand, we have recently also studied the structure-directing effect of (1R,2S)-dimethyl-ephedrinium and (1S,2S)-dimethyl-pseudoephedrinium for the synthesis of silica-based zeolite materials.<sup>37</sup> Interestingly, we found notable differences in the structure-directing behavior of the two closely-related diastereoisomers: the (1R,2S)-isomer was able to direct the crystallization of a layered crystalline precursor with ferrierite layers, while the (1S,2S)-isomer did not produce any crystalline material under the same conditions, despite their very similar molecular structure. These chiral cations combine a strong molecular asymmetry (due to the presence of 2 stereogenic centers) and a number of freely-rotating single bonds which provide a rich conformational space. Indeed, it has been shown by us<sup>37,38</sup> and others<sup>39-41</sup> that the conformational behavior of organic SDAs can be crucial during the structure-directing phenomenon of zeolite materials. Furthermore, diastereoisomerism can also have a strong influence on the crystallization path.<sup>42-44</sup> This has motivated us to perform a comparative systematic study of the structure-directing effect of the two chiral diastereomeric quaternary cations, (1R,2S)-dimethyl-ephedrinium (DMEP) and (1S,2S)-dimethyl-pseudoephedrinium (DMPS) (see Figure 1-top for the molecular structure), during the synthesis of nanoporous aluminophosphate materials. Moreover, we perform a combined study by <sup>13</sup>C NMR and quantum mechanics simulations in order to unravel the conformational space of these diastereoisomeric chiral cations, both in solution and when confined within the nanoporous space of a zeolite framework.

## **Experimental and Computational Details**

### *A) Synthesis of SDAs*

Synthesis of the quaternary cation (1R,2S)-dimethyl-ephedrinium hydroxide (DMEP) has been described in our previous work.<sup>35</sup> Synthesis of (1S,2S)-dimethyl-

pseudoephedrinium (DMPS) was carried out similarly; details are given in the Supporting Information.

#### *B) Synthesis of nanoporous materials*

Nanoporous aluminophosphate materials (AFI framework type) were prepared by hydrothermal methods using DMEP and DMPS as SDAs from gels with composition: 1 SDA : 0.22 MO : 0.89 Al<sub>2</sub>O<sub>3</sub> : 1 P<sub>2</sub>O<sub>5</sub> : 50 H<sub>2</sub>O, where M was Mg, Zn, Co or Si. Pseudoboehmite (Pural SB-1 77.5% Al<sub>2</sub>O<sub>3</sub>, Sasol), phosphoric acid (Sigma-Aldrich, 85%), magnesium acetate Mg(CH<sub>3</sub>COO)<sub>2</sub>·4H<sub>2</sub>O (Sigma-Aldrich, 99%), zinc acetate Zn(CH<sub>3</sub>COO)<sub>2</sub>·2H<sub>2</sub>O (Sigma-Aldrich, 98%), cobalt acetate Co(CH<sub>3</sub>COO)<sub>2</sub>·4H<sub>2</sub>O (Sigma-Aldrich, 98%) and tetraethylorthosilicate TEOS (Si(CH<sub>3</sub>CH<sub>2</sub>O)<sub>4</sub>, Merck 99%) were used as sources of Al, P, Mg, Zn, Co and Si, respectively. The gels were transferred into Teflon-lined stainless steel autoclaves with a capacity of 14 mL, which were heated statically at temperatures of 140 and 180 °C under autogenous pressure for 24 hours. The resulting solids were collected by filtration, washed thoroughly with ethanol and water and dried at room temperature.

#### *C) Characterization of nanoporous materials*

The obtained solids were characterized by powder X-Ray Diffraction (XRD), using a Philips X'PERT diffractometer with CuK<sub>α</sub> radiation with a Ni filter, with a step size of 0.04° and 20s time step, 0.04 rad soller slit, 45 kV voltage and 40 mA current. Thermogravimetric analyses (TGA) were registered using a Perkin-Elmer TGA7 instrument (heating rate = 20 °C/min) under air flow. UV–Visible diffuse reflectance spectroscopy was recorded with a UV-Vis Cary 5000 Varian spectrophotometer equipped with an integrating sphere, using the synthetic polymer Spectralen as reference. MAS-NMR spectra were recorded with a Bruker AV 400 WB spectrometer; details are given in the Supporting Information.

The aggregation state of the organic cations within the AFI solid samples was studied by fluorescence spectroscopy. Solid state UV-Visible fluorescence emission spectra were recorded in a RF-5300 Shimadzu fluorimeter. The fluorescence spectra were registered in the front-face configuration by a solid sample holder in which the samples were oriented 30 and 60° with respect to the excitation and emission beams, respectively. Fluorescence spectra of the solid samples were recorded by means of thin films supported on glass slides elaborated by solvent evaporation from a CH<sub>2</sub>Cl<sub>2</sub> suspension of the solid samples.

#### *D) Computational Details*

The conformational space of DMEP and DMPS was scanned by means of the Conformers Calculation Module in Materials Studio,<sup>45</sup> optimising the molecular structures for each set of dihedral angles. Calculation of the stability of these conformers in vacuum was then performed at *ab-initio* level with the Gaussian09 code,<sup>46</sup> using DFT and the hybrid B3LYP functional (including the D3 Grimme dispersion term); a 6-311G++(d,p) basis set was employed. The stability of these conformers was also calculated using plane-waves as basis set, and the PBE generalized gradient approximation as functional,<sup>47</sup> as implemented in the CASTEP module<sup>48</sup> in Materials Studio. Besides, the stability of such conformers was also determined by molecular mechanics using different combinations of force-fields and atomic charge-distributions. Results showed that molecular mechanics models using the pcff force-field<sup>49,50</sup> and atomic charge-distributions obtained from DFT+D calculations (using the B3LYP hybrid functional and the ESP charge calculation method), reproduced well the energy results of the conformational space calculated at the B3LYP level, and hence this combination was selected for force-field calculations.

The conformational behaviour of the two cations in water was studied by NVT Molecular Dynamics simulations, in the same way as reported in our previous works.<sup>38,51</sup> 16 organic cations, 16 Cl<sup>-</sup> anions (for charge-compensation) and 800 water molecules were included in the simulation cell (in the same ratio as in the gels used for the synthesis of MgAPO-5), and 250 ps of MD simulations in the NVT ensemble were run at 298 K. The conformational behaviour of the cations was studied by analysing the Radial Distribution Functions (RDF) of selected sets of atoms.

The most stable location of the different conformers of the chiral organic cations within the Mg-containing AFI framework has been studied by a combination of molecular mechanics and DFT calculations. The molecules were initially loaded in the corresponding AFI system using the pcff force-field. The framework charges were fixed to -1.2 for O, 3.4 for P, 1.4 for Al and 0.4 for Mg. The AFI structure was initially optimised with the GULP code,<sup>52</sup> using the potential developed by Catlow,<sup>53</sup> and Galen and Henson.<sup>54</sup> This optimised AFI framework was then used for studies of docking and packing of the DMEP cations using the Forcite module, as implemented in Materials Studio;<sup>49</sup> these calculations were performed keeping the coordinates of the framework atoms fixed. In order to determine the most stable packing of the cations within the one-dimensional channels, 1x1x6 AFI supercells were used, which allowed to study different rotations between consecutive cations (following the hexagonal symmetry of the AFI framework). The organic cations were manually docked in the required orientation; one Mg cation per organic cation was introduced (by replacement of Al) in the closest position to the molecular hydroxyl group of the organic cations in each case, and the systems were geometry optimised. This allowed us to study rather big systems which enabled the analysis of very different packing arrangements between the several conformers of the SDA cations.



Once determined the most stable packing arrangements of the conformers of DMEP and DMPS in the AFI channels, these systems were finally geometry-optimized at the DFT+D level, using the CASTEP module; no constraints were included in these calculations. The final interaction energies were obtained by subtracting the energy of the isolated framework and organic cations to the total energy of the system; all energies are reported in kcal/mol per AFI unit cell.

Calculation of the NMR chemical shielding of the different conformers were performed with the gauge-including projector augmented-wave method (GIPAW) developed by Pickard and Mauri.<sup>55</sup> The chemical shift for a nucleus in a given position ( $\delta(r)$ ) is defined as:

$$\delta(r) = \sigma_{\text{ref}} - \sigma(r)$$

where  $\sigma(r)$  is the isotropic shielding obtained in the calculations. In order to compare with the experimental  $^{13}\text{C}$  chemical shifts, we chose a  $\sigma_{\text{ref}}$  of 176 ppm as in our previous work,<sup>39</sup> so that the theoretical and experimental chemical shifts of the most shielded nuclei roughly coincide. In this way, we calculated the  $^{13}\text{C}$  NMR chemical shifts of the different DMEP and DMPS conformers, both in vacuo and confined within the AFI systems, and compared with the experimental values. Averaged values for  $^{13}\text{C}$  calculated chemical shifts with several equivalent atoms are reported.

## Results

### Synthesis and Characterization of Aluminophosphates

#### A) *MgAPO solids*

The different crystalline products identified in the solids are reported in Table 1. In the case of Mg as dopant, at the low crystallization temperature of 140 °C, both cations, DMEP and DMPS, produce pure MgAPO-5 materials (see Figure S1 for the XRD patterns). However, when the crystallization temperature is increased to 180 °C,

MgAPO-5 materials are still obtained, although some differences caused by the SDA used are raised. MgAPO-5 obtained with DMPS is more crystalline, although there is a minor amount of small-pore SOD phase accompanying the solid. In the case of DMEP, the amount of MgAPO-5 is lower, while the amount of the SOD phase is slightly higher, and there is also a minor presence of the small-pore AWO phase; the crystallization of both SOD and AWO might be a consequence of small degradation products of the chiral cations.

The incorporation of the organic cations within the framework was studied by  $^{13}\text{C}$  CP MAS NMR (Figure 1); liquid  $^{13}\text{C}$  NMR of the corresponding ammonium iodides in  $\text{CD}_3\text{OD}$  are also shown for comparison (in black). We observe that all the resonances of the salts in solution are present in the MgAPO-5 solids in both cases, though some of the bands are slightly shifted due to confinement effects. If we take a close inspection to the resonance corresponding to C1 of DMEP confined within the AFI framework (as labelled in Figure 1), we observe two clearly distinguishable bands at 7.7 and 14.7 ppm, one of them close to the resonance of this C atom in solution (at 6.0 ppm). As we previously reported,<sup>35</sup> the two bands show up in all the MgAPO-5 materials prepared under very different synthesis conditions (Figure S2), with a similar intensity. When the crystallization temperature was increased, some degradation products start to show up, giving resonances at ~45-49 ppm and 58 ppm (Figure 1), which are not present at 140 °C. Hence, it seems that at 140 °C the DMEP cations are intact, and as a consequence the additional band at 14.7 ppm has to be assigned to DMEP cations, possibly in different configurations due to the confinement within the one-dimensional channels of the AFI framework. Interestingly, the situation is different for DMPS: in this case, we observe one main band at 15.5 ppm when confined within the AFI structure, which is shifted with respect to the band in solution at 12.5 ppm (the same occurs when MgAPO-

5 is obtained at 180 °C); in addition, we observe a small shoulder at 10-14 ppm, though with a lower intensity. This particular NMR behavior might be related to the high conformational flexibility of these molecules, and will be the subject of a computational DFT study below.

Thermogravimetric analyses of MgAPO-5 materials obtained at 140 °C (not shown) suggest an organic content of ~1.0-1.1 SDAs/u.c. (note that this number must be slightly overestimated because of the overlapping of dehydroxylation processes). The presence of an aromatic ring in the SDA cations involves that they can be incorporated within the AFI channels as monomers or dimers.<sup>31</sup> UV-Vis fluorescence spectroscopy was applied in order to study the supramolecular aggregation of these cations when occluded within the AFI solids (Figure 2). Both MgAPO-5 materials obtained at 140 °C with DMEP and DMPS show a main band with a vibronic structure centered at 284 nm (top-left), which is assigned to the incorporation of the SDA cations as monomers, without  $\pi$ - $\pi$  stacking. The incorporation of dimers, revealed by the broad band between 350-380 nm, is very minor in these materials.

The incorporation of Mg into the AFI framework in the MgAPO-5 materials was verified by <sup>31</sup>P MAS NMR (Figure S3), which showed a band at -30 ppm assigned to P(4Al), and another band at -24 ppm assigned to P(1Mg,3Al), evidencing the incorporation of Mg into the AFI tetrahedral network.

#### *B) CoAPO solids*

The introduction of Co in the synthesis gels also lead to the crystallization of pure CoAPO-5 materials in the presence of both cations at 140 °C (see Table 1 and Figure S4). Instead, when the crystallization temperature is increased to 180 °C, CoAPO-5 crystallized in the presence of DMEP together with the GIS phase (CoAPO-43).<sup>56,57</sup> The GIS framework has small 8-ring channels, which points to be the result of the

degradation of the DMEP cations at high temperature. Indeed, the CoAPO-43 phase has been previously obtained after in-situ degradation of large amines.<sup>56</sup> In the case of the sample obtained with DMPS at 180 °C, crystallization of CoAPO-5 is very poor, and is accompanied by CoAPO-GIS and -SOD phases, again as a consequence of degradation of the DMPS cations.

Fluorescence spectroscopy (Figure 2-top-right) shows the predominance of SDAs occluded as monomers (band at 282 nm), although in this case the presence of SDA dimers is somewhat higher than in MgAPO-5 materials. The incorporation of Co within the AFI tetrahedral network was verified by UV-Visible diffuse reflectance spectroscopy (Figure S5), showing three bands at 540, 580 and 624 nm characteristic of tetrahedral Co<sup>2+</sup>.<sup>58</sup>

### *C) ZnAPO solids*

In the presence of Zn in the synthesis gels, XRD results (Figure S6) show similar trends as before (Table 1): ZnAPO-5 materials are obtained at low temperature. In addition, the material obtained with DMEP showed an additional peak at 4.7° 2θ, which probably comes from the presence of a low-dimensional material (possibly also displaying a peak at 20.5° 2θ), and that with DMPS showed a very minor presence of GIS. Again an increase of the crystallization temperature results in a complex mixture of phases, with ATN (ZnAPO-39),<sup>59</sup> SOD (ZnAPO-20) and GIS (ZnAPO-43) (probably as a result of the structure-directing effect of degradation products) accompanying the AFI phase when the sample is obtained in the presence of DMEP, and AFI, SOD and to a minor extent GIS and AWO when the SDA used is DMPS (Table 1). Fluorescence spectroscopy of the ZnAPO-5 materials obtained at 140 °C (Figure 2-bottom-left) again shows a major incorporation of the SDA cations as monomers.

#### *D) SAPO solids*

The incorporation of Si in the synthesis gels makes more difficult the crystallization of the AFI phase (see Figure S7). SAPO-5 materials crystallize at 140 °C with both cations, although their crystallinity is relatively low. In the case of using DMEP as SDA, SAPO-5 crystallizes together with a minor amount of AlPO-tridymite, while with DMPS a low-dimensional phase (XRD peak at  $4.5^\circ 2\theta$ ) accompanies the AFI material (Table 1). In contrast, SAPO-5 crystallization occurs only to a minor extent when the crystallization temperature is increased to 180 °C, and only when DMEP is the SDA. The main crystalline product in both cases is SAPO-20, with the SOD framework (Figure S7-right); indeed, this is the main crystalline phase observed from the gel prepared with DMPS (though with an impurity of AWO). Of course the SOD framework, which is composed of fused sodalite cages, is not able to host the large SDA cations, and hence it must be a consequence of the degradation of the cations.

In order to analyze the organic species that directed the crystallization of the SOD phase, we registered the  $^{13}\text{C}$  CP MAS NMR spectra of the two SAPO materials obtained at 180 °C (Figure 3). The SAPO-SOD material obtained with DMPS (right) gave only two resonance signals at 58.2 and 46.8 ppm. The former is typical of tetramethylammonium (TetraMA) cations confined within AlPO sodalite cages,<sup>60</sup> while the latter is in the range typical of trimethylamine (TriMA); no other signals that could be assigned to the original DMPS cation are observed. In the case of the SAPO material obtained with DMEP, the same two  $^{13}\text{C}$  resonances at 58.2 and 46.8 ppm are observed, indicative of the presence of the same two species. In addition, in this material some bands (at around 130 and 54 ppm) with minor intensity are still observed, which can be assigned to the presence of some DMEP remnant species in the minor amount of SAPO-5 phase (Figure S7). Indeed, the relative ratio of the two bands is different in the

two materials. UV-Vis fluorescence spectra of SAPO-5 materials obtained at 140 °C (Figure 3, bottom-right) shows again the major incorporation of monomers within the AFI framework.

#### *E) AlPO solids*

In the absence of dopants, AlPO-5 crystallizes with the two SDA cations, but together with some unknown low-dimensional phases and AlPO-trydimite (Figure S8). In contrast, when the crystallization temperature is increased to 180 °C, a crystalline material related to AlPO-12-TAMU (ATT) crystallizes with both SDAs (Figure S8-right). <sup>13</sup>C MAS NMR spectra of these samples (Figure S9) displayed two signals at 46.2 and 47.8 ppm, in the typical region of trimethylamine, and another two at 56.8 and 56.4 ppm, in the typical region of tetramethylammonium, suggesting the occlusion of both species within the ATT framework. Indeed, AlPO-12-TAMU (ATT) was originally obtained with tetramethylammonium.<sup>61</sup>

#### **Study of the degradation of DMEP and DMPS**

Our results so far suggest a lower hydrothermal stability of DMPS, especially during the synthesis of SAPO materials. In order to study this difference between the two diastereomeric cations, we prepared aqueous solutions of the two SDA cations (as hydroxides), neutralized with equimolar amounts of HCl, in a molar ratio of  $1\text{SDA}^+(\text{OH}^-):1\text{HCl}:40\text{H}_2\text{O}$ . These solutions were then subjected to hydrothermal treatments (in autoclaves) at 100 and 150 °C for several periods of time (1, 3 or 10 days); liquid <sup>13</sup>C NMR spectra of the resulting solutions (after the heating treatment) were then recorded. The <sup>13</sup>C NMR spectra of solutions subjected to the thermal treatment at 100 °C (Figure S10) showed no degradation of DMEP, even after 10 days. In the case of DMPS, some new NMR peaks start to appear after 3 days, at 44.8, 23.8 and 19.3 ppm. After 10 days, the intensity of these peaks increases, and new peaks

appear at 49.2 ppm. This result provides a clear indication that DMPS displays a lower thermal stability than DMEP. Of all these peaks, we could only identify the one at 44.8 ppm as tentatively assigned to trimethylamine (in fact, protonated trimethylammonium since neutral trimethylamine would appear at higher shifts, at ~46.7 ppm). However, at this temperature we did not observe peaks at ~55 ppm which would correspond to tetramethylammonium cations.

At 150 °C, differences in the stability of the two diastereoisomers are more apparent (Figure S11). Degradation of DMPS at this higher treatment is much more evident, especially after 10 days, where lots of new resonance peaks show up, while DMEP remains still pretty much unaltered. Hence we focus on the thermal degradation of DMPS. Even after just 1 day, a prominent peak starts to appear at 44.8 ppm; at the same time, some other peaks show up at 78.4, 71.2, 18.2 and 10.3 ppm (among others with lower intensity). Worth is noting a peak at 55.2 ppm, which can be tentatively assigned to tetramethylammonium. These new signals increase their intensity with time, and besides some other new signals appear, evidencing the progress of the degradation process. Indeed, if we plot the relative area (normalized to the number of C) of the signals assigned to trimethylamine (TriMA, blue) and tetramethylammonium (TetraMA, red) (Figure S12), we can clearly observe that TriMA is first formed, and its production increases with time; TetraMA is only produced at 150 °C, and after an induction period (once TriMA has been produced), and then after three days its formation is notably increased. These results suggest that the evolution of DMPS involves first the formation of TriMA (upon degradation of DMPS through Hofmann elimination), and this is then transformed (via transfer of methyl groups from remnant DMPS) to TetraMA. Villaescusa et al. have recently reported the same degradation mechanism for N,N,N-trimethyl-tert-butylammonium, which is first degraded to

trimethylamine (through Hofmann elimination), and then this reacts with further N,N,N-trimethyl-tert-butylammonium through a transmethylation reaction to finally yield tetramethylammonium, promoting the segregation of two closely similar AST phases with slightly different unit cell parameters (the first hosting N,N,N-trimethyl-tert-butylammonium and the second hosting tetramethylammonium).<sup>62</sup>

Surprisingly, despite the closely similar molecular structure of the two diastereoisomers, we have found a notably lower stability of the (1S,2S)-isomer (DMPS) than that of (1R,2S)-DMEP. This could be tentatively explained by the different stereochemical configuration of the hydroxyl group, which facilitates the attack of a base (required for the Hofmann elimination) in the case of DMPS and/or prevent it in the case of DMEP (see Figure S13).

## **Computational Results**

As mentioned previously, the characterization of MgAPO-5 materials showed a particular NMR behavior of the bands corresponding to C1 for the two isomers occluded within the AFI framework (Figure 1), which might be related to the high conformational flexibility of these molecules. For this reason, we performed a subsequent computational study in order to unravel the confinement of these chiral species within the channels of the AFI framework.

### *A) Conformational Analysis*

First of all we looked at the conformational space of the two cations (in vacuo) as a function of their stereochemical configuration (Figure 4). The relative energies of the different conformers in vacuo have been calculated with different levels of theory, and results are in very good agreement (Table 2). For both cations, the most stable conformer in vacuo is A, with an open configuration of the alkyl chain in which the bulky groups (trimethylammonium and phenyl) are opposite to each other (in ‘anti’



configuration), giving an elongated molecular shape (see Figure 4-top). In conformers B and C, the ammonium and phenyl bulky groups are close to each other ('syn' configuration), giving place to a steric hindrance which results in a lower stability (by more than 2 kcal/mol). In the case of DMEP, conformer B, where H and the phenyl ring are in 'anti' configuration, the hydroxyl and ammonium groups are in 'syn' configuration, giving a higher stability, while for DMPS, conformer C, where the methyl (bonded to the asymmetric C) is 'anti' to the phenyl ring, is more stable (than B) because it is in this conformation where the hydroxyl and ammonium groups are in 'syn' configuration (see Table 2 and Figure 4).

We calculated the NMR chemical shieldings of these isomers in vacuo (at DFT+D/PBE level) (Table 3). We clearly observe that C1 (corresponding to the methyl group attached to the asymmetric C atom, see Figure 1) is the C atom whose chemical shift is mostly influenced by the conformation adopted. In the case of DMEP, conformers A, B and C give C1 chemical shifts of 6.3, 13.3 and 11.2 ppm, respectively. Indeed, if we compare with the  $^{13}\text{C}$  chemical shift of DMEP<sup>+</sup> iodide dissolved in CD<sub>3</sub>OD (or in aqueous solution, see Figure S14), we realize that the experimental value is very similar to that calculated for conformer A, suggesting that conformer A is the one occurring in solution. This is in good agreement with the higher stability observed for this conformer in vacuo (Table 2). Therefore, our results suggest that the C1 chemical shift can be used to monitor the occurrence of the different DMEP conformations.

In the case of DMPS, again the chemical shift of C1 is the most strongly influenced by the conformation adopted, although in this case the different stereochemical configuration involves distinct chemical shifts (Table 3). Conformers A, B and C give theoretical C1 chemical shifts of 11.7, 5.3 and 15.3 ppm, respectively. The experimental  $^{13}\text{C}$  chemical shift for C1 in solution is 12.3 ppm, which again is very similar to the one

calculated for conformer A, suggesting also the preferential occurrence of conformer A in solution. Once again this is in very good agreement with the higher stability calculated for DMPS conformer A in vacuo (Table 2). The reason for the different calculated chemical shifts of conformer A observed for the two diastereoisomers, DMEP (6.3 ppm) and DMPS (11.7 ppm) (Table 3), is the different stereochemical relative configuration of C1 with respect to the hydroxyl group, which is in ‘syn’ configuration in DMEP and ‘anti’ in DMPS (see Figure 4-top), giving place to different chemical environments and hence distinct chemical shieldings.

#### *B) MD simulations in water*

We next studied through molecular dynamics simulations the conformational behavior of the two cations in water (using the pcff force-field model). Systems with the same SDA/H<sub>2</sub>O ratio (1:50) as in the synthesis gels were built, and the occurrence of the different conformations was monitored by calculating RDFs of selected distances (see Table S1 for the interatomic distances which define the different conformers). Conformers A (of both DMEP and DMPS) display a C1...N distance of ~4.1 Å, while this distance is reduced to 3.3-3.4 Å for conformers in folded configuration (B and C). Intramolecular RDF between C1 and N atoms during the MD simulations (Figure S15, left) shows a main peak at ~4.1 Å for both diastereoisomers, evidencing that conformer A is the one that mostly occur in aqueous solution; a minor peak at 3.3 Å is also observed, which reveals a minor presence of a folded conformer. <sup>13</sup>C NMR of aqueous solutions of DMEP<sup>+</sup> and DMPS<sup>+</sup> iodide salts (Figure S14) show C1 resonances which nicely fit those theoretically calculated for conformer A of both diastereoisomers, in good agreement with the major presence of this conformer in aqueous solution. On the other hand, intermolecular RDFs between aromatic C (cp) atoms (Figure S15-right) do not display a peak at ~4 Å, clearly showing a low supramolecular aggregation (through

$\pi$ - $\pi$  type interactions) trend of these cations, which can also explain the low incorporation of dimers within the AFI channels (as observed by fluorescence spectroscopy).

### *C) Confinement within AFI*

We then studied the confinement of the different conformers of both diastereoisomers within the one-dimensional channels of the AFI framework in the presence of Mg. UV-Vis fluorescence spectroscopy results had shown that both cations incorporate within the AFI structure as monomers (without interaction between the aromatic rings of adjacent SDA cations) (Figure 2, top-left).<sup>35</sup> Hence, we modelled the packing of both DMEP and DMPS cations within the AFI channels as monomers in a head-to-tail configuration under a packing value of 1.0 SDA per u.c. (as revealed by TGA).

First of all, we studied if there is any influence of the SDA hydrophilic groups (OH and  $\text{NMe}_3^+$ ) on the location of Mg dopants embedded in the AFI framework (note that doping through replacement of  $\text{Al}^{3+}$  by  $\text{Mg}^{2+}$  involves the generation of a negative charge on the network which is compensated by the organic SDA cation). With this purpose, we loaded 1 DMEP cation per AFI u.c. with 1 Mg (replacing Al), and rotated the SDA cation around the channel axis so that to get different distances between the hydrophilic groups (OH and  $\text{NMe}_3^+$ ) and Mg; we expect these hydrophilic groups to interact more strongly with the negative charge associated to Mg in the framework. The relative energies were obtained by DFT+D (PBE) geometry-optimization of the systems. We did this for conformers A and B of DMEP. Relative energy results (in kcal/mol per AFI u.c.) are reported in Figure 5, expressed as a function of the  $\text{H(O)}\cdots\text{Mg}$  (left) or  $\text{N}^+\cdots\text{Mg}$  (middle) distance for conformer A (top) and B (bottom). If we look at the  $\text{H(O)}\cdots\text{Mg}$  distance (left), we appreciate a clear relationship with the energy, where lower distances give higher stabilities, and an increase in this distance

comprises a notable reduction of the stability. This occurs both for conformers A and B, although it is more prominent for conformer A. In contrast, no such clear relationship is observed between the stability and the  $N^+ \cdots Mg$  distance (middle). This is due to the bulky nature of the  $NMe_3^+$  group, where the positive charge of N is rather shielded by the three methyl groups, preventing a strong interaction with the negative charge associated to Mg. Therefore, it becomes clear that Mg will prefer to site close to the molecular hydroxyl group, establishing strong H-bonds between organic H(O) groups and framework O(Mg) atoms in order to maximize electrostatic interactions (as is the case in the most stable situation, highlighted with dashed circles in Figure 5-left, and shown at right for both conformers).

We next studied the packing of the SDA cations within the AFI channels. In order to find the best packing orientation between consecutive SDA cations while preventing artifacts imposed by the periodicity of the model, and considering the hexagonal symmetry of the AFI channels, we built 1x1x6 supercells, in which adjacent cations were consecutively rotated (around the channel axis) by the same angle of  $\pm n \cdot 60^\circ$  (for  $n = 0, 1, 2, 3$ ; i.e. giving angles between consecutive cations of  $-120^\circ, -60^\circ, 0^\circ, +60^\circ, +120^\circ$  and  $+180^\circ$ ). In addition, two possible orientations of the cations along the channel axis (related by  $180^\circ$ -turn perpendicular to the channel axis) were studied (referred as ‘+c’ and ‘-c’) (Figure S16). Following our previous observation, Mg atoms were always located in the Al position closest to the molecular OH group, thus following the packing pattern of the organic SDA. The very large number of systems (6 rotation angles and 2 orientations for each of the three conformers, giving a total of 36 system for DMEP and 36 for DMPS) and the very large size of the models (with 636 atoms) forced us to use forcefield (pcff) calculations in this part of the study. Figure S17 shows the relative energy (for each SDA cation) in the different conformations and orientations

as a function of the packing angle between consecutive cations. In general, conformers A and B of DMEP pack more efficiently with no-rotation (angle  $0^\circ$ ) or  $-60^\circ$ -rotation between consecutive cations, while conformer C prefers to pack with a rotation of  $+120^\circ$ . Something similar occurred with the packing of DMPS cations within the AFI channels (Figure S17-bottom, in blue). Both conformers A and B pack more efficiently with no rotation or  $-60^\circ$ -rotation between consecutive cations, while the most stable packing of conformer C involves  $-60$  and  $180^\circ$  for (+c) and (–c) orientations, respectively. The most stable orientations for each conformer were then geometry-optimized at DFT+D/PBE level (using supercells adequate to the symmetry of each system, see Tables 4 and 5).

DFT+D energies for DMEP cations confined within the AFI channels in different conformations and orientations are reported in Table 4 (Figure 6 shows the location of the most stable configuration for each conformer). Packing of conformer A is more stable in (–c) orientation; in this case, the most stable packing involves the cations rotated consecutively by  $-60^\circ$  (with an interaction energy of  $-181.8$  kcal/mol), thus developing a helicoidal supramolecular organic arrangement that is indeed transferred into a helicoidal distribution of Mg through the  $\text{OH}\cdots\text{Mg}$  coupled incorporation (Figure 6-top, DMEP-A-(–c)– $60^\circ$ ). DMEP conformers (A) confined within the AFI channels give a theoretical  $\delta$  (C1) of 7-8 ppm (Table 4). The most stable packing of conformer B involves no rotation between consecutive cations (and hence with Mg always in the same position, Figure 6), being slightly more stable in (–c) orientation, with an interaction energy of  $-179.3$  kcal/mol, notably lower than that of DMEP-A-(–c)– $60^\circ$ . Conformers B confined in the AFI channels give theoretical  $\delta$  (C1) around 14 ppm (Table 4). Finally, the most stable packing of C conformers (this was the least stable in vacuo) involves a rotation between consecutive cations of  $+120^\circ$ , and resulting in an

equivalent arrangement of the Mg ions within the AFI framework (Figure 6). The (+c) orientation is more stable, giving an interaction energy of -179.7 kcal/mol, which is again smaller than that of conformers A. The organic arrangement with DMEP in conformation C gives theoretical  $\delta$  (C1) values of 16-17 ppm (Table 3). In sum, these DFT energy results would predict a preferential incorporation of DMEP as conformer A in an helicoidal ordered fashion where consecutive cations would be rotated by  $-60^\circ$ .

However, if we take  $\delta$  (C1) as an indication of the occurrence of the different DMEP conformers, we observe that the previous prediction does not match the experimental observations since the experimental  $^{13}\text{C}$  NMR spectra of MgAPO-5 materials obtained with DMEP displayed always two distinct signals with similar intensity assigned to C1 at  $\sim 7$  ppm and  $\sim 14$  ppm (Figure 1), which should be indicative of a simultaneous occurrence of conformers A and B. Indeed, we note that, regardless of the synthesis conditions of the material, the intensity of the two resonances is always very similar (see Figure S2), suggesting a paired occurrence of both conformers in the MgAPO-5 materials. Following this observation, we also studied theoretically Mg-AFI systems that were loaded with both conformers A and B (in a 1:1 ratio) in an alternate fashion ( $\text{A}\cdots\text{B}\cdots\text{A}\cdots\text{B}$ ), again with Mg located in the closest positions to the hydroxyl groups of both conformers (systems A+B in Table 4). Pcff calculations showed that the most stable packing arrangement in this hybrid system involved also no rotation between consecutive DMEP cations (Figure S17), though due to the presence of the two distinct conformers, Mg now sites in consecutive unit cells in positions related by  $60^\circ$  rotation (Figure 6-bottom). DFT+D geometry-optimization of this Mg-AFI-DMEP system with the two conformers (A+B) gave the highest interaction energy of all systems (-182.3 kcal/mol for (+c) orientation), being even more stable than conformer A in (-c) orientation. This clearly indicates that this paired occurrence of conformers A and B of

DMEP in a 1:1 alternate fashion provides the best packing efficiency of this cation within the AFI channels. Calculation of the  $\delta$  (C1) of this system would predict the occurrence of two resonances with the same intensity at 5.2 and 12.9 ppm, in excellent agreement with the experimental observations. For the sake of completeness, we also studied the simultaneous incorporation of conformers A+C, but in this case the systems were less stable (Table 4).

We next studied the incorporation of the DMPS diastereoisomer; Table 5 reports energy results for the different systems studied, and the most stable ones are shown in Figure 7. The most stable packing arrangements of conformers A and B are the same as those of DMEP, with conformer A being more efficiently packed in (–c) orientation with a consecutive rotation between cations of  $-60^\circ$  (with an interaction energy of -177.9 kcal/mol and a theoretical  $\delta$  (C1) of 13 ppm), and conformer B in (+c) orientation with no rotation between cations (giving an interaction energy of -179.8 kcal/mol and a theoretical  $\delta$  (C1) of 9 ppm) (Table 5). However, in contrast to DMEP, in this case the most stable packing arrangement of DMPS (without considering combination of conformers) involves conformers C in (–c) orientation, where consecutive cations are rotated by  $180^\circ$  (Figure 7), giving an interaction energy of -180.7 kcal/mol and a  $\delta$  (C1) of 17.6 ppm. These results would predict a preferential incorporation of DMPS as conformer C. Indeed, if we look at the experimental  $^{13}\text{C}$  NMR, we observe a high intensity of the signal at ~16 ppm (Figure 1), suggesting the preferential occurrence of DMPS as conformer C, in good agreement with this theoretical prediction. As in the previous case for DMEP, we also studied the simultaneous incorporation of combinations of conformers (A+B and A+C). As for DMEP, the packing of A+B conformers in an alternate fashion gives the highest stability (with interaction energies of -181.2 and -181.6 kcal/mol for (+c) and (–c) orientations, see Table 5) (Figure 7-

bottom), being slightly more stable than conformer C (by less than 1 kcal/mol). If this was the case, DFT calculations would predict the occurrence of two  $^{13}\text{C}$  NMR signals at around 10 and 14 ppm (for (+c) orientation) or 7 and 11 ppm (for (–c) orientation), with similar intensities (Table 5). However, experimental  $^{13}\text{C}$  NMR shows a much better comparison with the sole occurrence of conformer C (with a predicted single signal at around 17 ppm) than a combination of A and B, and hence we propose the former case to be responsible for the  $^{13}\text{C}$  NMR spectrum. Nonetheless, we can appreciate also a broad band between 10-14 ppm (though with a lower intensity) that could indicate some presence of (A+B) conformers in this configuration.

## Discussion

Our combined experimental  $^{13}\text{C}$  NMR and computational simulations study has revealed that the conformational space of (1R,2S)-dimethyl-ephedrinium and (1S,2S)-dimethyl-pseudoephedrinium can be monitored by the NMR resonance of one particular C atom in these cations (C1); related conformation-dependences of the  $^{13}\text{C}$  NMR signals have also been reported for other zeolitic systems.<sup>39</sup> Our results show that the conformational space of these chiral cationic species is altered by confinement within nanoporous spaces. In vacuo and in aqueous solution, both cations display a unique conformation with an open configuration of the alkyl chain (conformer A). However, confinement within the one-dimensional channels of the AFI framework provides a higher stability to the folded conformations, probably due to a higher interaction and better packing efficiency under such conformations. In the case of DMEP, the most stable packing efficiency occurs with a 1:1 mixture of conformers A and B. We have recently reported the crystallization of a ferrierite-related layered material using the same DMEP cation as SDA (ICP-1 and PREFER).<sup>37</sup> Molecular simulations showed that in these materials, DMEP cations prefer to site in conformation A (see Figure S18).



Interestingly, this material gives a unique C1 resonance at 6 ppm (Figure S19), in very good agreement with our assignment of this band to conformer A of DMEP. Therefore, it becomes clear that confinement of the SDA cations within different nanoporous spaces can definitely alter the conformational space, providing stability to conformers that are not stable in open spaces (in vacuo or in solution).

Confinement of the other diastereoisomer, DMPS, also influences the conformational space of the cation. As for DMEP, the most stable packing arrangement of this isomer involves a simultaneous incorporation of conformers A and B. However, the experimental NMR spectrum seems to indicate a favored incorporation of the next (in term of interaction energy) stable system, with single conformers C, in contrast with the observations for DMEP. The lower occurrence of (A+B)-configuration for DMPS could be explained by the very low stability of conformer B of DMPS in vacuo (being 4 kcal/mol less stable than conformer A, as determined by B3LYP, see Table 2), which would prevent (from kinetics considerations) the occurrence of conformer B prior to confinement during crystallization, and as a consequence this would impede such combined (A+B) packing arrangement. In contrast, conformer B is less unfavored for DMEP (being only 2.5 kcal/mol less stable in vacuo, Table 2), which explains the occurrence of this (A+B) combination for this isomer. We note also here that calculations of the MgAFI-DMPS systems are performed with PBE functional, which tends to overestimate the stability of conformer B in DMPS (see Table 2, which overestimates the stability of B by 1.5 kcal/mol with respect to B3LYP), and hence the real stability of (A+B)-DMPS (Table 5) might be overestimated.

Finally, we briefly discuss the implications of our work on the production of chiral materials through helicoidal arrangements of dopants. We have seen that the presence of hydroxyl groups in the SDA cations seems to favor a coupled incorporation of the

dopants, which tend to locate close to the OH molecular group because of the establishment of H-bond interactions enhanced by the negative charge associated to the isomorphic substitution of the dopant. At the same time, we have observed that under certain configurations, supramolecular helicoidal arrangements of the cations represent the most efficient packing configurations, especially for conformers A (in (–c) orientations). Combined with the coupled incorporation of dopants, this could give place to the occurrence of helicoidal distributions of dopants embedded in the AFI network. However, theoretical energy results combined with NMR data indicate that these helicoidal organic configurations of conformer A do not actually occur, but other non-chiral configurations are more stable.

## Conclusions

In this work we have performed a comparative study of the structure-directing effect of two chiral diastereoisomers, (1R,2S)-dimethylephedrinium and (1S,2S)-dimethylpseudoephedrinium, in the synthesis of nanoporous aluminophosphates. At low temperature, both chiral isomers promote the crystallization of the AFI framework doped with different metals, with the organic cations confined within the channels mainly as monomer species. However, an increase of the crystallization temperature to 180 °C triggers a partial degradation of the organic cations through Hofmann elimination to give first trimethylamine, which is then further transformed by transmethylation reactions to tetramethylammonium, resulting in the formation of small-pore/cavity-based frameworks. Because of the different stereochemical configuration, such degradation occurs to a larger extent in the (1S,2S)-dimethylpseudoephedrinium cation.

Molecular simulations show a different conformational space of the two isomers as a function of their stereochemical configuration. The combination of theoretical DFT

calculations and  $^{13}\text{C}$  NMR spectroscopy has allowed us to assign the resonances of a particular C atom with the occurrence of the different conformations of the two diastereoisomers. As a consequence, we have been able to monitor the occurrence of the different conformations in aqueous solution and within the Mg-AFI systems. We have observed that one particular conformer (A), with the alkyl chain in an open-configuration, is clearly the most favored one in aqueous solution, while this is not the case when the organic cations are confined within the one-dimensional nanopores of the AFI framework. In this case, a different situation is found for the two isomers as a function of their stereochemical configuration: packing of the (1R,2S)-isomer involves a simultaneous occurrence of conformers A and B in an alternated fashion, giving place to two  $^{13}\text{C}$  NMR signals with similar intensities, while packing of (1S,2S)-isomers involves the sole incorporation of a different conformer (C). Finally, we remark the relevance of combining molecular simulation methods with experimental NMR characterization of the solids in order to gain deep insights on the host-guest chemistry of nanoporous materials. Our study and the findings achieved here could be also very helpful to understand and predict molecular recognition events in drug-receptor systems related with conformational chemistry, which could potentially be monitored by  $^{13}\text{C}$  NMR, as we have shown in this work.

### **Supporting Information**

Organic synthesis details, NMR experiments details, XRD patterns, UV-Vis diffuse reflectance spectroscopy, additional NMR studies, interatomic distances used to monitor the occurrence of conformers, additional molecular pictures, Radial Distribution Functions and energy diagrams, are included as Supporting Information.

## Acknowledgements

This work has been partially financed by the Spanish Ministry of Economy, Industry and Competitiveness (Project MAT2015-65767-P) and the Spanish State Research Agency (Agencia Española de Investigación, AEI) and the European Regional Development Fund (Fondo Europeo de Desarrollo Regional, FEDER) through the Project MAT2016-77496-R (AEI/FEDER, UE). BBM acknowledges the Spanish Ministry of Economy and Competitiveness for a predoctoral (BES-2013-064605) contract. Secretaría General Adjunta de Informática-CSIC is acknowledged for running the calculations, and BIOVIA for providing the computational software.

## References

- (1) Davis, M. E. New vistas in zeolite and molecular sieve catalysis. *Acc. Chem. Res.* **1993**, *26*, 111-115.
- (2) Cejka, J. ; Corma, A. ; Zones, S. I. Zeolites and catalysis: synthesis reactions and applications. Wiley-VCH Verlag GmbH & Co. KGaA **2010**.
- (3) Davis, M. E. Ordered porous materials for emerging applications. *Nature* **2002**, *417*, 813-821
- (4) Smit, B.; Maesen, T. L. M. Towards a molecular understanding of shape selectivity. *Nature* **2008**, *451*, 671-678.
- (5) Vogt, E. T. C.; Weckhuysen, B. M. Fluid catalytic cracking: recent developments on the grand old lady of zeolite catalysis. *Chem. Soc. Rev.* **2015**, *44*, 7342-7370.
- (6) Abate, S.; Barbera, K.; Centi, G.; Lanzafame, P.; Perathoner, S. Disruptive catalysis by zeolites. *Catal. Sci. Technol.* **2016**, *6*, 2485-250.
- (7) Wilson, S. T.; Lok, B. M.; Flanigen, E. M. U.S. Patent 4,310,440, **1982**.
- (8) Corà, F.; Alfredsson, M.; Barker, C. M.; Bell, R. G.; Foster, M. D.; Saadoune, I.; Simperler, A.; Catlow, C. R. A. Modeling the framework stability and catalytic activity of pure and transition metal-doped zeotypes. *J. Solid State Chem.* **2003**, *176*, 496-529.
- (9) Burton, A. W.; Zones, S. I. Organic molecules in zeolite synthesis: their preparation and structure-directing effects. *Stud. Surf. Sci. Catal.* **2007**, *168*, 137-179.

- (10) Kubota, Y.; Helmkamp, M. M.; Zones, S. I.; Davis, M. E. Properties of organic cations that lead to the structure-direction of high-silica molecular sieves. *Microporous Mater.* **1996**, *6*, 213-229.
- (11) Moliner, M.; Rey, F.; Corma, A. Towards the rational design of efficient organic structure-directing agents for zeolite synthesis. *Angew. Chem. Int. Ed.* **2013**, *52*, 13880-13889.
- (12) Lew, C. M.; Davis, T. M.; Elomari, S. Synthesis of new molecular sieves using novel structure-directing agents (Chapter 2). In: Mintova S (ed) Verified syntheses of zeolitic materials, 3rd revised edition. Published on behalf of the Synthesis Commission of the International Zeolite Association 2016, pp 29–35. ISBN: 978-0-692-68539-6.
- (13) Gómez-Hortigüela, L.; Cambor, M. A. Introduction to the zeolite structure-directing phenomenon by organic species: General aspects. In: Gómez-Hortigüela L. (eds) Insights into the chemistry of organic structure-directing agents in the synthesis of zeolitic materials. Structure and Bonding, vol 175. Springer, Cham.
- (14) Lawton, S. L.; Rohrbaugh, W. J. The Framework Topology of ZSM-18, a novel zeolite containing rings of three (Si,Al)-O species. *Science* **1990**, *247*, 1319-1322.
- (15) Moliner, M.; González, J.; Portilla, M. T.; Willhammar, T.; Rey, F.; Llopi, F. J.; Zou, X.; Corma, A. A new aluminosilicate molecular sieve with a system of pores between those of ZSM-5 and beta zeolite. *J. Am. Chem. Soc.* **2011**, *133*, 9497-9505.
- (16) Davis, M. E. Reflections on routes to enantioselective solid catalysts. *Top. Catal.* **2003**, *25*, 3-7.
- (17) Yu, J.; Xu, R. Chiral zeolitic materials: structural insights and synthetic challenges *J. Mat. Chem.* **2008**, *18*, 4021-4030.
- (18) Van Erp, T. S.; Caremans, T. P.; Dubbeldam, D.; Martín-Calvo, A.; Calero, S.; Martens, J. A. Enantioselective adsorption in achiral zeolites. *Angew. Chem. Int. Ed.* **2010**, *49*, 3010-3013.
- (19) Castillo, J. M.; Vlugt, T. J. H.; Dubbeldam, D.; Hamad, S.; Calero, S. Performance of chiral zeolites for enantiomeric separation revealed by molecular simulation. *J. Phys. Chem. C* **2010**, *114*, 22207-22213.
- (20) Morris, R. E.; Bu, X. H. Induction of chiral porous solids containing only achiral building blocks. *Nat. Chem.* **2010**, *2*, 353-361.
- (21) Dubbeldam, D.; Calero, S.; Vlugt, T. J. H. Exploring new methods and materials for enantioselective separations and catalysis. *Molec. Sim.* **2014**, *40*, 585-598.

- (22) Harris, K. D. M.; Thomas, S. J. M. Selected thoughts on chiral crystals, chiral surfaces, and asymmetric heterogeneous catalysis. *ChemCatChem*. **2009**, *1*, 223-231.
- (23) Treacy, M. M. J.; Newsam, J. M. 2 New 3-dimensional 12-ring zeolite frameworks of which zeolite beta is a disordered intergrowth. *Nature* **1988**, *332*, 249-251.
- (24) Rajic, N.; Logar, N. Z.; Kaucic, V. A novel open framework zincophosphate - synthesis and characterization. *Zeolites* **1995**, *15*, 672-678.
- (25) Sun, J.; Bonneau, C.; Cantín, A.; Corma, A.; Díaz-Cabañas, M. J.; Moliner, M.; Zhang, D.; Li, M.; Zou, X. The ITQ-37 mesoporous chiral zeolite. *Nature* **2009**, *458*, 1154-1157.
- (26) Rojas, A.; Cambor, M. A. A pure silica chiral polymorph with helical pores. *Angew. Chem. Int. Ed.* **2012**, *51*, 3854-3856.
- (27) Tang, L. Q.; Shi, L.; Bonneau, C.; Sun, J. L.; Yue, H. J.; Ojuva, A.; Lee, B. L.; Kritikos, M.; Bell, R. G.; Bacsik, Z.; Mink, J.; Zou, X. D. A zeolite family with chiral and achiral structures built from the same building layer. *Nat. Mater.* **2008**, *7*, 381-385.
- (28) Gómez-Hortigüela, L.; Bernardo-Maestro, B. Chiral organic structure-directing agents. In: Gómez-Hortigüela L. (eds) Insights into the chemistry of organic structure-directing agents in the synthesis of zeolitic materials. Structure and Bonding, vol 175. Springer, Cham.
- (29) Brand, S. K.; Schmidt, J. E.; Deem, M. W.; Daeyaert, F.; Ma, Y.; Terasaki, O.; Orazov, M.; Davis, M. E. Enantiomerically enriched, polycrystalline molecular sieves. *Proc. Natl. Acad. Sci.* **2017**, *114*, 5101-5106.
- (30) Álvaro-Muñoz, T.; López-Arbeloa, F.; Pérez-Pariente, J.; Gómez-Hortigüela, L. (1R,2S)-Ephedrine: A new self-assembling chiral template for the synthesis of aluminophosphate frameworks. *J. Phys. Chem. C* **2014**, *118*, 3069-3077.
- (31) Bernardo-Maestro, B.; López-Arbeloa, F.; Pérez-Pariente, J.; Gómez-Hortigüela, L. Comparison of the structure-directing effect of ephedrine and pseudoephedrine during crystallization of nanoporous aluminophosphates. *Microporous Mesoporous Mater.* **2017**, *254*, 211-224.
- (32) Bernardo-Maestro, B.; Roca-Moreno, M. D.; López-Arbeloa, F.; Pérez-Pariente, J.; Gómez-Hortigüela, L. Supramolecular chemistry of chiral (1R,2S)-ephedrine confined within the AFI framework as a function of the synthesis conditions. *Catal. Today* **2016**, *277*, 9-20.

- (33) Gómez-Hortigüela, L.; Álvaro-Muñoz, T.; Bernardo-Maestro, B.; Pérez-Pariente, J. Towards chiral distributions of dopants in microporous frameworks: helicoidal supramolecular arrangement of (1R,2S)-ephedrine and transfer of chirality. *Phys. Chem. Chem. Phys.* **2015**, *17*, 348-357.
- (34) Gómez-Hortigüela, L.; Corà, F.; Pérez-Pariente, J. Chiral distributions of dopants in microporous materials: a new concept of chirality. *Microporous Mesoporous Mater.* **2012**, *155*, 14-15.
- (35) Bernardo-Maestro, B.; Vos, E.; López-Arbeloa, F.; Pérez-Pariente, J.; Gómez-Hortigüela, L. Supramolecular chemistry controlled by packing interactions during structure-direction of nanoporous materials: effect of the addition of methyl groups on ephedrine derivatives. *Microporous Mesoporous Mater.* **2017**, *239*, 432-443.
- (36) Database of Zeolite Structures. <http://www.iza-structure.org/databases>, accessed on 1<sup>st</sup> Aug 2018.
- (37) Gálvez, P.; Bernardo-Maestro, B.; Vos, E.; Díaz, I.; López-Arbeloa, F.; Pérez-Pariente, J.; Gómez-Hortigüela, L. ICP-2: A new hybrid organo-inorganic ferrierite precursor with expanded layers stabilized by  $\pi$ - $\pi$  stacking interactions. *J. Phys. Chem. C* **2017**, *121*, 24114-24127.
- (38) Bernardo-Maestro, B.; López-Arbeloa, F.; Pérez-Pariente, J.; Gómez-Hortigüela, L. Supramolecular chemistry controlled by conformational space during structure-direction of nanoporous materials: self-assembly of ephedrine and pseudoephedrine. *J. Phys. Chem. C* **2015**, *119*, 28214-28225.
- (39) Lu, P.; Gómez-Hortigüela, L.; Xu, L.; Cambor, M. A. Synthesis of STW zeolite using imidazolium-based dications of varying length. *J. Mater. Chem. A* **2018**, *6*, 1485-1495.
- (40) O'Brien, M. G.; Beale, A. M.; Catlow, C. R. A.; Weckhuysen, B. M. Unique organic-inorganic interactions leading to a structure-directed microporous aluminophosphate crystallization as observed with in situ Raman spectroscopy. *J. Am. Chem. Soc.* **2006**, *128*, 11744-11745.
- (41) Sánchez-Sánchez, M.; Sankar, G.; Gómez-Hortigüela, L. NMR evidence of different conformations of structure-directing cyclohexylamine in high-doped AlPO<sub>4</sub>-44 materials. *Microporous Mesoporous Mater.* **2008**, *114*, 485-494.
- (42) Tsuji, K.; Beck, L. W.; Davis, M. E. Synthesis of 4,4'-trimethylenebis(1-benzyl-1-methylpiperidinium) diastereomers and their use as structure-directing agents in pure-silica molecular sieves syntheses. *Microporous Mesoporous Mater.* **1999**, *28*, 519-530.

- (43) Lee, G. S.; Nakagawa, Y.; Hwang, S.-J.; Davis, M. E.; Wagner, P.; Beck, L.; Zones, S. I. Organocations in zeolite synthesis: fused bicyclo [l.m.0] cations and the discovery of zeolite SSZ-48. *J. Am. Chem. Soc.* **2002**, *124*, 7024-7034.
- (44) García, R.; Gómez-Hortigüela, L.; Sánchez, F.; Pérez-Pariente, J. Diastereoselective structure directing effect of (1S,2S)-2-Hydroxymethyl-1-benzyl-1-methylpyrrolidinium in the synthesis of ZSM-12. *Chem. Mater.* **2010**, *22*, 2276-2286.
- (45) Conformer Calculation module, Material Studio, **2017** R2, BIOVIA.
- (46) Frisch, M. J. Gaussian 09, Revision D.01, Gaussian, Inc., Wallingford CT, **2013**.
- (47) Perdew, J. P.; Burke, K.; Ernzerhof, M. Generalized Gradient Approximation made simple. *Phys. Rev. Lett.* **1996**, *77*, 3865-3868.
- (48) Clark, S. J.; Segall, M. D.; Pickard, C. J.; Hasnip, P. J.; Probert, M. J.; Refson, K.; Payne, M. C. First principles methods using CASTEP. *Z. Kristallogr.* **2005**, *220*, 567-570.
- (49) Forcite Calculation module, Material Studio, **2017** R2, BIOVIA.
- (50) Sun, H.; Mumby, S. J.; Maple, J. R.; Hagler, A. T. An ab Initio CFF93 all-atom force field for polycarbonates. *J. Am. Chem. Soc.* **1994**, *116*, 2978-2987.
- (51) Gómez-Hortigüela, L.; Hamad, S.; Pinar, A. B.; López-Arbeloa, F.; Pérez-Pariente J.; Corà, F. Molecular insights into the self-aggregation of aromatic molecules in the synthesis of nanoporous aluminophosphates: a multilevel approach. *J. Am. Chem. Soc.* **2009**, *131*, 16509-16524.
- (52) Gale, J. D.; Rohl, A. L. The General Utility Lattice Program (GULP). *Mol. Simulat.* **2003**, *29*, 291-341.
- (53) Schroder, K. P.; Sauer, J.; Leslie, M.; Catlow, C.R.A.; Thomas. J. M. Bridging hydroxyl groups in zeolitic catalysts: a computer simulation of their structure, vibrational properties and acidity in protonated faujasites (H<sup>+</sup> · Y zeolites) *Chem. Phys. Lett.* **1992**, *188*, 320-325.
- (54) Gale, J. D.; Henson, N. J. Derivation of interatomic potentials for microporous aluminophosphates from the structure and properties of berlinite. *J. Chem. Soc. Faraday Trans.* **1994**, *90*, 3175-3179.
- (55) Pickard, C. J.; Mauri, F. All-electron magnetic response with pseudopotentials: NMR chemical shifts. *Phys. Rev. B*, **2001**, *63*, 245101.
- (56) Feng, P.; Bu, X.; Stucky, G. D. Hydrothermal syntheses and structural characterization of zeolite analogue compounds based on cobalt phosphate. *Nature* **1997**, *388*, 735-741.



- (57) Feng, P.; Bu, X.; Gier, T. E.; Stucky, G. D. Amine-directed syntheses and crystal structures of phosphate-based zeolite analogs. *Microporous Mesoporous Mater.* **1998**, *23*, 221-229.
- (58) Urbina de Navarro, C.; Machado, F.; López, M.; Maspero, D.; Pérez-Pariente, J. A SEM/EDX study of the cobalt distribution in CoAPO-type materials. *Zeolites* **1995**, *15*, 157-163.
- (59) Christensen, A. N.; Jensen, T. R.; Norby, P.; Hanson, J. C. In situ synchrotron X-Ray powder diffraction studies of crystallization of microporous aluminophosphates and  $\text{Me}^{2+}$ -substituted aluminophosphates. *Chem. Mater.* **1998**, *10*, 1688-1693.
- (60) Li, D.; Xu, Y.; Ma, H.; Xu, R.; Wang, Y.; Liu, H.; Wang, B.; Tian, Z. Ionothermal syntheses of transition-metal-substituted aluminophosphate molecular sieves in the presence of tetraalkylammonium hydroxides. *Microporous Mesoporous Mater.* **2015**, *210*, 125-132.
- (61) Rudolf, P. R.; Saldarriaga-Molina, C.; Clearfield, A. Preparation and X-Ray powder structure solution of a novel aluminum phosphate molecular sieve,  $(\text{AlPO}_4)_3 \cdot (\text{CH}_3)_4\text{NOH}$ . *J. Phys. Chem.* **1986**, *90*, 6122-6125.
- (62) Villaescusa, L. A.; Cambor, M. A. Time evolution of an aluminogermanate zeolite synthesis: Segregation of two closely similar phases with the same structure type. *Chem. Mater.* **2016**, *28*, 3090-3098.

## Tables

Table 1. Crystalline phases obtained in the different solids, as determined by XRD. (↓) and (↓↓) indicates a minor and very minor presence, respectively. ‘LD’ refers to low-dimensional materials, ‘Try’ to AlPO-trydinite, and ‘U’ to unidentified phases.

| M    | Mg  |                           | Co  |                            | Zn             |                                      | Si               |                | ---                    |               |
|------|-----|---------------------------|-----|----------------------------|----------------|--------------------------------------|------------------|----------------|------------------------|---------------|
| SDA  | 140 | 180                       | 140 | 180                        | 140            | 180                                  | 140              | 180            | 140                    | 180           |
| DMEP | AFI | AFI<br>SOD(↓↓)<br>AWO(↓↓) | AFI | AFI<br>GIS(↓)              | AFI<br>LD(↓)   | AFI(↓)<br>ATN(↓)<br>SOD(↓)<br>GIS(↓) | AFI(↓)<br>Try(↓) | AFI(↓)<br>SOD  | AFI<br>LD(↓)<br>Try(↓) | AFI(↓)<br>ATT |
| DMPS | AFI | AFI<br>SOD(↓↓)            | AFI | AFI(↓)<br>GIS(↓)<br>SOD(↓) | AFI<br>GIS(↓↓) | AFI<br>SOD<br>GIS(↓)<br>AWO(↓↓)      | AFI(↓)<br>LD(↓)  | SOD<br>AWO(↓↓) | AFI<br>LD(↓)           | ATT<br>U      |

Table 2. Relative energies of the different conformers of DMEP and DMPS, calculated at different levels of theory (DFT+D at B3LYP and PBE levels, and molecular mechanics with pcff force-field).

| Conformer | Configuration | Relative Energy (kcal/mol) |     |      |       |     |      |
|-----------|---------------|----------------------------|-----|------|-------|-----|------|
|           |               | DMEP                       |     |      | DMPS  |     |      |
|           |               | B3LYP                      | PBE | pcff | B3LYP | PBE | pcff |
| <b>A</b>  | Open          | 0.0                        | 0.0 | 0.0  | 0.0   | 0.0 | 0.0  |
| <b>B</b>  | Folded        | 2.5                        | 2.1 | 2.0  | 4.0   | 2.5 | 4.5  |
| <b>C</b>  | Folded        | 4.1                        | 3.2 | 3.2  | 1.9   | 1.3 | 2.2  |

Table 3. Calculated chemical shifts (in ppm) for the different conformers of DMEP and DMPS in vacuo, calculated at DFT+D/PBE level (A, B and C), and experimental liquid <sup>13</sup>C chemical shifts of DMEP<sup>+</sup> and DMPS<sup>+</sup> iodides in CD<sub>3</sub>OD (Experm.). Labels are the same as in Figure 1.

| Cation      | Conformer      | C1          | C3          | C4          | C2          | C6           | C7           | C8           | C5           |
|-------------|----------------|-------------|-------------|-------------|-------------|--------------|--------------|--------------|--------------|
| <b>DMEP</b> | A              | 6.3         | 53.8        | 81.2        | 84.9        | 128.4        | 136.0        | 137.7        | 141.1        |
|             | B              | 13.3        | 54.5        | 84.9        | 82.5        | 129.2        | 136.2        | 137.9        | 138.6        |
|             | C              | 11.2        | 54.5        | 81.9        | 84.3        | 131.3        | 136.8        | 138.9        | 143.2        |
|             | <b>Experm.</b> | <b>6.0</b>  | <b>51.7</b> | <b>69.4</b> | <b>74.7</b> | <b>125.5</b> | <b>127.5</b> | <b>128.2</b> | <b>141.2</b> |
| <b>DMPS</b> | A              | 11.7        | 54.4        | 85.8        | 84.3        | 130.6        | 136.6        | 139.0        | 142.2        |
|             | B              | 5.3         | 53.6        | 78.1        | 81.7        | 132.0        | 136.0        | 138.5        | 139.4        |
|             | C              | 15.3        | 56.2        | 84.8        | 82.0        | 126.2        | 135.9        | 135.9        | 144.4        |
|             | <b>Experm.</b> | <b>12.3</b> | <b>52.6</b> | <b>73.9</b> | <b>74.9</b> | <b>127.3</b> | <b>128.4</b> | <b>128.6</b> | <b>141.9</b> |

Table 4. MgAFI-DMEP systems studied at DFT+D level; interaction energies (I. E.), and relative energies (R. E., with respect to the most stable case) are expressed in kcal/mol per u.c. Theoretical chemical shifts of C1 ( $\delta$  C1, in ppm) are also reported.

Note: \* indicates that  $\delta$  C1 has been calculated with smaller systems (with no intermolecular rotation in 1x1x1 u.c. AFI systems).

| Conformer        | Orientation | Rotation | Space group     | Supercell | I.E./u.c. | R.E./u.c. | $\delta$ C1 (ppm) |
|------------------|-------------|----------|-----------------|-----------|-----------|-----------|-------------------|
| <b>A</b>         | (+c)        | 0        | P1              | 1x1x1     | -179.0    | 3.2       | 6.6               |
| A                | (-c)        | -60      | P6 <sub>5</sub> | 1x1x6     | -181.8    | 0.4       | 7.8*              |
| <b>B</b>         | (+c)        | 0        | P1              | 1x1x1     | -178.7    | 3.5       | 14.3              |
| <b>B</b>         | (-c)        | 0        | P1              | 1x1x1     | -179.3    | 3.0       | 13.6              |
| <b>C</b>         | (+c)        | 120      | P3 <sub>1</sub> | 1x1x3     | -179.7    | 2.6       | 17.2*             |
| C                | (-c)        | 120      | P3 <sub>1</sub> | 1x1x3     | -176.0    | 6.2       | 16.1*             |
| <b>0.5A+0.5B</b> | (+c)        | 0        | P1              | 1x1x2     | -182.3    | 0.0       | 12.9/5.2          |
| <b>0.5A+0.5B</b> | (-c)        | 0        | P1              | 1x1x2     | -179.9    | 2.3       | ---               |
| <b>0.5A+0.5C</b> | (+c)        | 60       | P1              | 1x1x6     | -178.3    | 4.0       | ---               |
| <b>0.5A+0.5C</b> | (-c)        | 60       | P1              | 1x1x6     | -177.6    | 4.7       | ---               |

Table 5. MgAFI-DMPS systems studied at DFT+D level; interaction energies (I. E.), and relative energies (R. E., with respect to the most stable case) are expressed in kcal/mol per u.c. Theoretical chemical shifts of C1 ( $\delta$  C1, in ppm) are also reported.

Note: \* indicates that  $\delta$  C1 has been calculated with smaller systems (with no intermolecular rotation in 1x1x1 u.c. AFI systems).

| Conformer        | Orientation | Rotation | Space group     | Supercell | I.E./u.c. | R.E./u.c. | $\delta$ C1 (ppm) |
|------------------|-------------|----------|-----------------|-----------|-----------|-----------|-------------------|
| <b>A</b>         | (+c)        | 0        | P1              | 1x1x1     | -176.7    | 4.9       | 12.2              |
| A                | (-c)        | -60      | P6 <sub>5</sub> | 1x1x6     | -177.9    | 3.7       | 13.1*             |
| <b>B</b>         | (+c)        | 0        | P1              | 1x1x1     | -179.8    | 1.8       | 9.1               |
| <b>B</b>         | (-c)        | 0        | P1              | 1x1x1     | -175.8    | 5.8       | 11.3              |
| <b>C</b>         | (+c)        | -60      | P6 <sub>5</sub> | 1x1x6     | -178.5    | 3.1       | 19.3*             |
| C                | (-c)        | 180      | P2 <sub>1</sub> | 1x1x2     | -180.7    | 0.9       | 17.6              |
| <b>0.5A+0.5B</b> | (+c)        | 0        | P1              | 1x1x2     | -181.2    | 0.3       | 14.0/9.9          |
| <b>0.5A+0.5B</b> | (-c)        | 0        | P1              | 1x1x2     | -181.6    | 0.0       | 11.3/7.0          |
| <b>0.5A+0.5C</b> | (+c)        | -60      | P6 <sub>5</sub> | 1x1x6     | -176.8    | 4.8       | ---               |
| <b>0.5A+0.5C</b> | (-c)        | 60       | P6 <sub>1</sub> | 1x1x6     | -176.6    | 5.0       | ---               |

## Figures

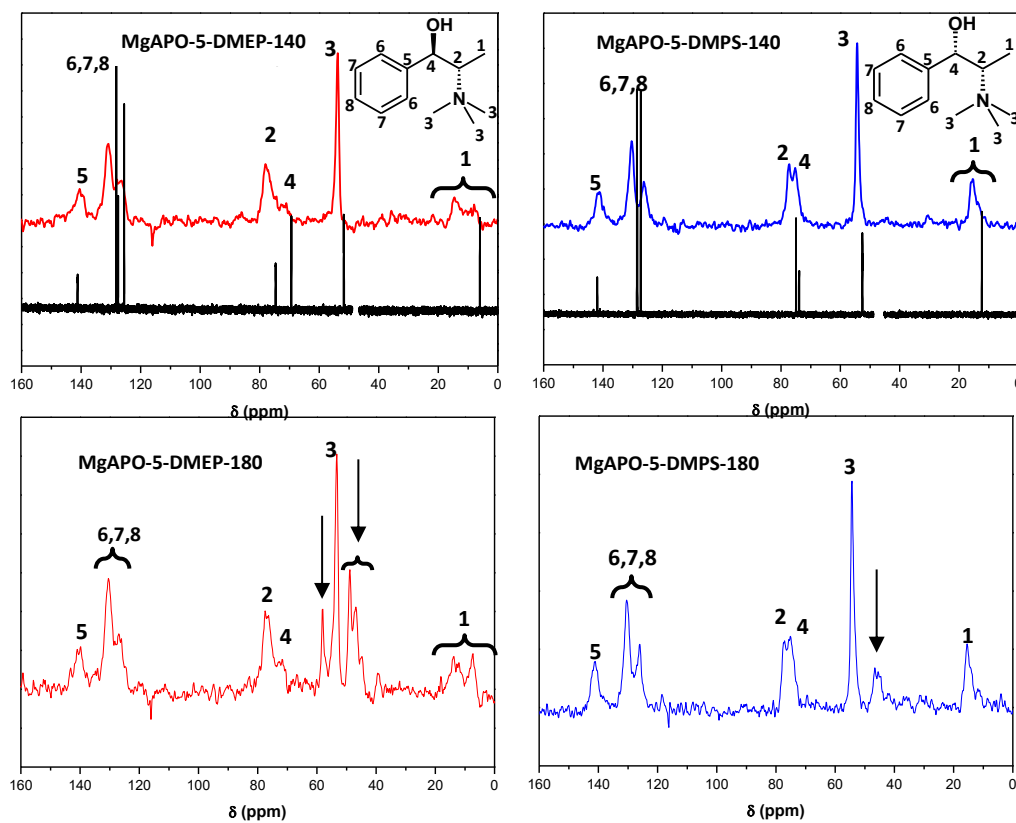


Figure 1.  $^{13}\text{C}$  CP MAS NMR spectra of MgAPO-5 materials obtained with DMEP (red) or DMPS (blue) at 140 °C (top) or 180 °C (bottom). Degradation products are indicated by arrows.

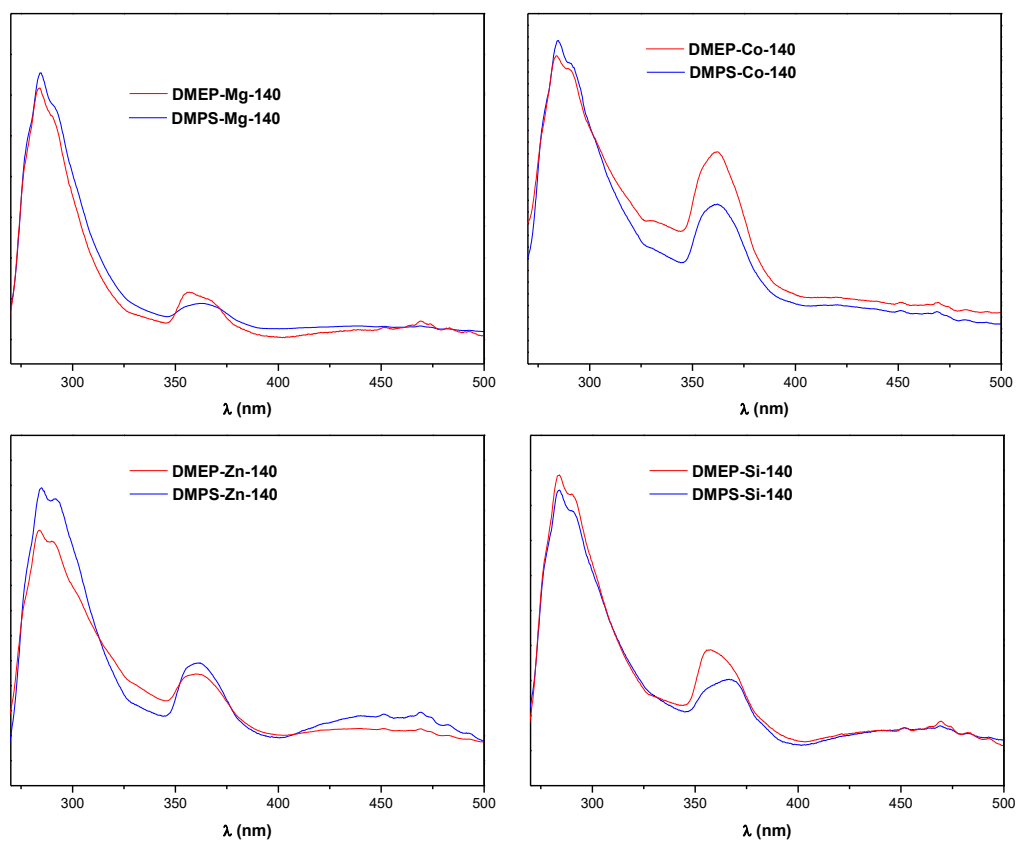


Figure 2. UV-Vis Fluorescence spectra of MAPO-5 materials obtained with DMEP (red) or DMPS (blue) as SDAs, in the presence of Mg (top-left), Zn (top-right), Co (bottom-left) or Si (bottom-right) at 140 °C.

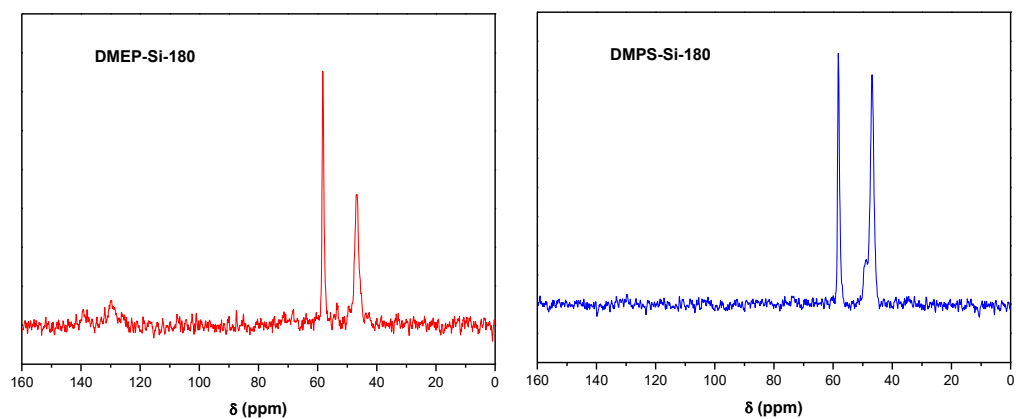


Figure 3.  $^{13}\text{C}$  CP MAS NMR spectra of SAPO materials obtained with DMEP (left) or DMPS (right) at 180 °C.

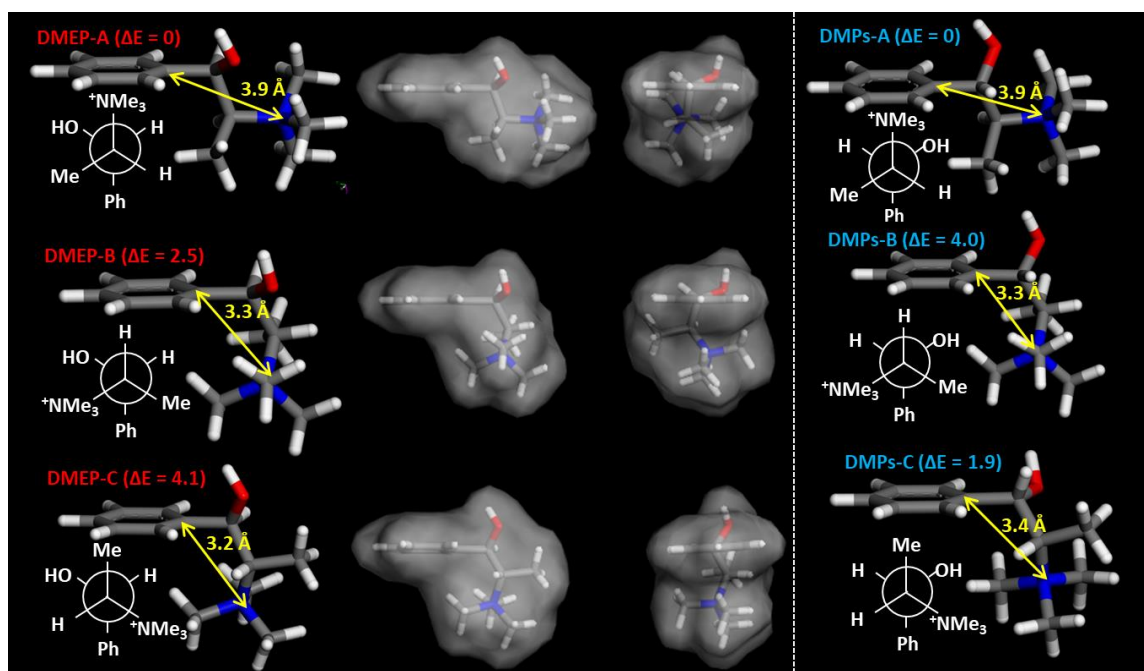


Figure 4. Molecular structure and relative energies (at DFT/B3LYP level, in kcal/mol) of different conformers of DMEP (left) and DMPsEP (right).

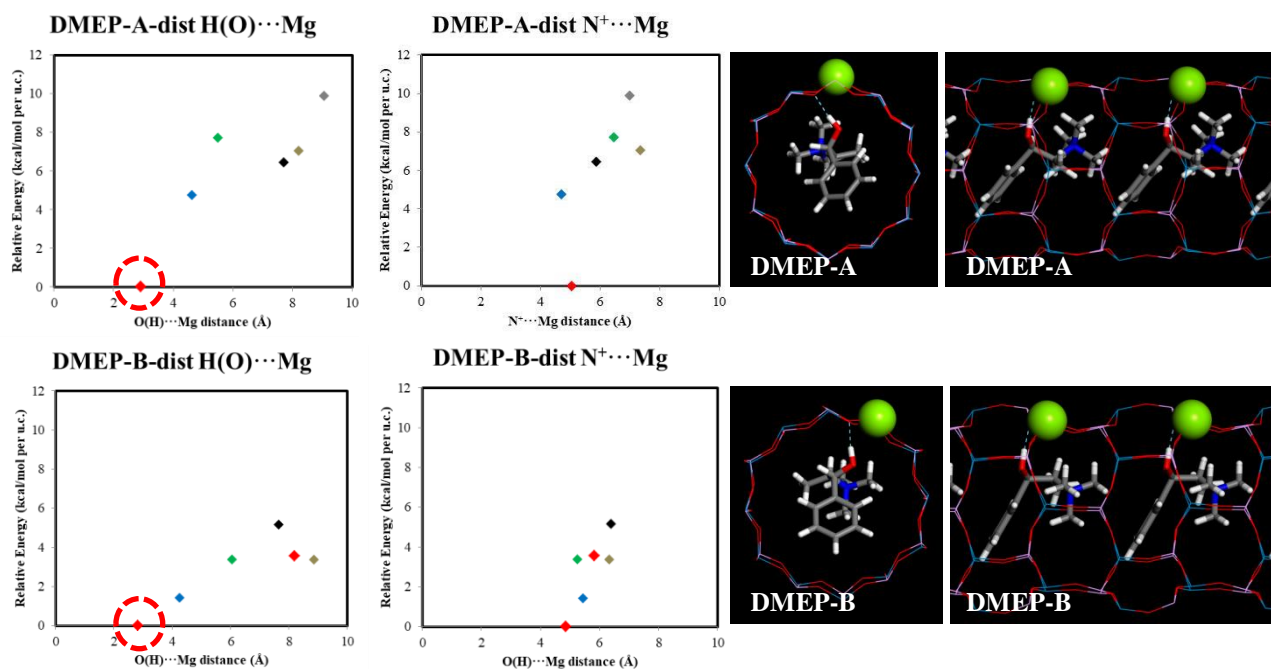


Figure 5. Relative energy (DFT+D/PBE, in kcal/mol per u.c.) of DMEP conformer A (top) or B (bottom) as a function of the distance between H(O) and Mg (left) or between N<sup>+</sup> and Mg (middle) (each system is shown in a different color); right: images of the most stable configurations for each DMEP conformer (corresponding to dashed circles to the right).



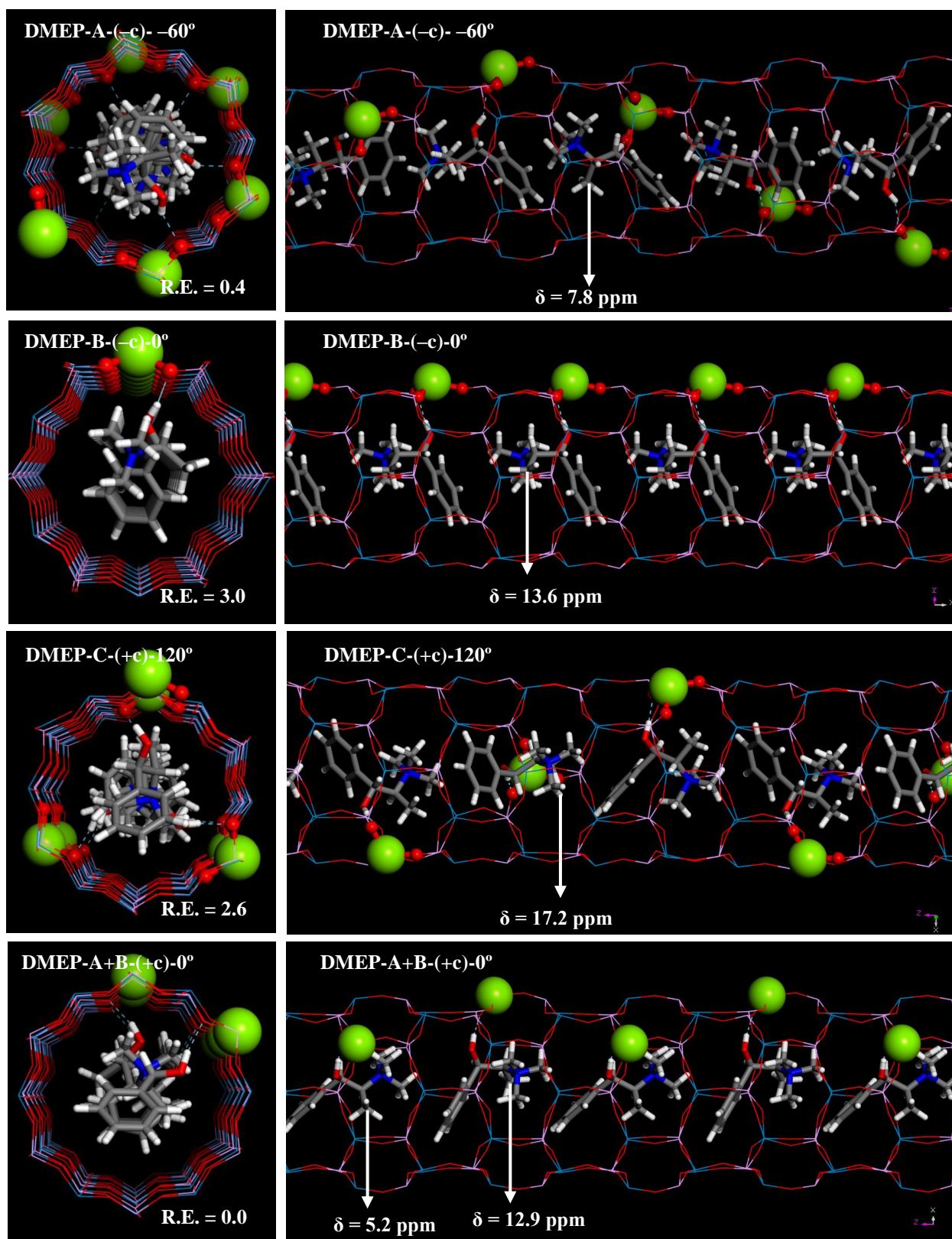


Figure 6. Location of DMEP cations in the different conformations and orientations. Relative energies (in kcal/mol per u.c.) and  $\delta$  (C1) are also reported.

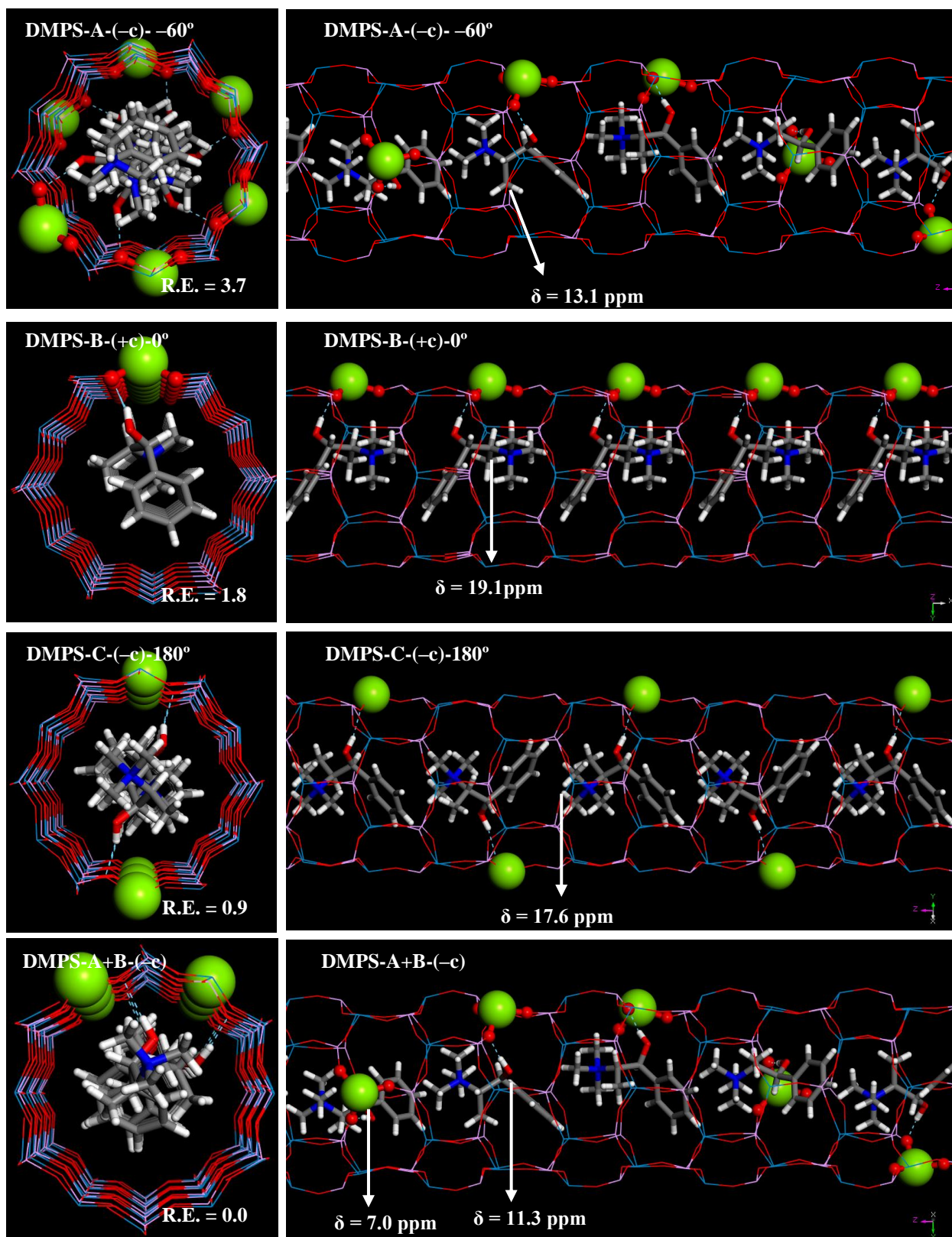


Figure 7. Location of DMPS cations in the different conformations and orientations. Relative energies (in kcal/mol per u.c.) and  $\delta$  (C1) are also reported.

## Table of Contents Image (TOC)

